Linear and nonlinear beam dynamics of vertical fixed-field accelerators

Marion Vanwelde,[1,*] Cédric Hernalsteens,[2,1,†] and Nicolas Pauly[1]

[1]*Service de Métrologie Nucléaire (CP165/84), Université libre de Bruxelles, Avenue Franklin Roosevelt 50, 1050 Brussels, Belgium*

[2]*CERN, European Organization for Nuclear Research, Esplanade des Particules 1, 1211 Meyrin, Switzerland*

(Received 1 September 2023; accepted 8 January 2024; published 15 February 2024)

Vertical fixed-field accelerators (vFFAs) feature a magnetic field that increases exponentially in the vertical direction, resulting in vertically stacked nonplanar orbits. Their magnetic field is highly nonlinear, and their solenoid and quadrupolar components induce strongly coupled optics. The detailed study of their beam dynamics must account for the transverse motion linear and nonlinear coupling. Specifically, the study of linear beam dynamics requires adequate coupling parametrizations, and the study of nonlinear beam dynamics, including the characterization of the dynamic aperture (DA), must be performed in the full 4D phase space. The ZGOUBI ray-tracing code is ideally suited to study the vFFA transverse dynamics, as it can perform step-by-step particle tracking in vFFA complex geometry and magnetic fields. This paper provides an in-depth study of the vFFA prototype ring designed under the ISIS-II proton driver prototype project to accelerate proton beams from 3 to 12 MeV. The magnets of this vFFA ring exhibit slow magnetic field falloffs, resulting in a significant influence of the neighboring cells on the optical lattice parameters. The determination of stable orbits and tunes requires superimposing 3D magnetic field maps in ZGOUBI to account for the neighboring cell residual fields. The study of nonlinear beam dynamics revealed the appearance of fourth-order stability islands. A complete characterization of the DA in the 4D phase space was conducted to give a measure of the stability domain and characterize the performance and limitations of this lattice. This study paves the way for further validation studies with experimental data and field maps.

DOI: 10.1103/PhysRevAccelBeams.27.024003

I. INTRODUCTION

Vertical fixed-field accelerators (vFFAs) [1–4] exhibit highly nonlinear magnetic fields that exponentially increase in the vertical direction. To maintain constant tunes during acceleration, the vFFA magnetic field satisfies the scaling condition $B = B_0 \exp[k(Z - Z_0)]$, where $k = (1/B)(\partial B/\partial Z)$ is the normalized field gradient, Z is the vertical coordinate in the Cartesian frame, Z_0 is a vertical reference position, and B_0 is the magnetic field strength at that reference position. Contrary to conventional horizontal excursion FFAs (hFFAs[1]), the vertical scaling condition does not determine the horizontal shape of the ring. The machine footprint can be smaller compared to hFFAs and uses taller magnets with simpler configurations. As the magnetic field increases in the vertical direction, the vFFAs present finite vertical dispersion but zero horizontal dispersion leading to a momentum compaction factor α_c strictly equal to zero. This is interesting for ultrarelativistic beams, as the independence of path length with the beam momentum allows for delivering continuous beams. Due to these many advantages, vFFAs have been considered for various applications, from nuclear waste transmutation to energy-recovery electron accelerators and synchrotron radiation sources [4,8]. As part of the ISIS Neutron and Muon Source Facility upgrade ("ISIS-II") [9–11], horizontal and vertical FFAs are considered for the 1.2 GeV proton driver of the neutron and muon source [12]. The construction of a prototype ring, where the ISIS Front End Test Stand (FETS) [13] serves as an injector,[2] is envisaged to demonstrate the viability of an FFA solution and validate the beam dynamics experimentally. In this context, a complete procedure to design such vFFA lattices has been proposed in Ref. [8], and a vFFA prototype ring

*marion.vanwelde@ulb.be

†cedric.hernalsteens@cern.ch

[1]Horizontal excursion FFAs magnetic field satisfies the scaling condition $B = B_0(r/r_0)^k$, where B_0 and r_0 are the reference field and radius, and $k = (r/B)(\partial B/\partial r)$ is the field index [5–7].

[2]In the following, we will refer to this prototype as "FETS-vFFA."

has been designed to accelerate proton beams from 3 to 12 MeV [8,14].

The vFFA magnetic field presents a nonzero longitudinal field due to the fringe fields at the vFFA element ends and skew quadrupolar components in the magnet body [8]. These components induce strongly coupled optics, and the linear beam dynamics must be studied with an adequate parametrization of the linear optics [15]. The generalized lattice functions can be obtained from two parametrization categories that allow either to find the linear invariants in the linearly decoupled phase spaces (Edwards and Teng parametrization) or to link them to measurable quantities, such as the beam sizes (Mais and Ripken parametrization). The vFFA magnetic field can be modeled using different fringe field functions. While the hyperbolic tangent function is often used to describe the field falloff in vFFA magnets [4,8,16], it has been shown that an arctangent function better describes the field falloff of realistic coil-dominated magnets [17]. It is thus essential to study vFFA lattices with this fringe field function to obtain simulation results that could predict experimental results. In the FETS-vFFA prototype ring, the magnet fringe fields have a predominant role as the prototype is a compact machine with small vFFA magnets, a large bending angle per cell, and an average radius of about 4.5 m. The arctangent fringe fields drop slowly to zero and impact the focusing strength experienced by the particles so that the residual fields of neighboring cells influence the cell optical parameters.

In addition to the linear transverse coupling and peculiarities of fringe fields, the magnetic field of vFFAs is also highly nonlinear, which induces nonlinear coupling between linearly decoupled planes. The detailed study of their nonlinear beam dynamics must thus consider linear and nonlinear coupling. In particular, the dynamic aperture (DA) corresponds to the stability domain in the 4D phase space. Although a measure of this stability domain can be helpful when comparing several machines, it does not characterize the phase space complexity and lacks a clear interpretable meaning in terms of beam injection, as it can significantly deviate from the acceptance hypersphere of the machine. Further analysis is thus required to have insights into the global system dynamics, its operating performances, and limitations in the coupled physical space [18].

Studying vFFA lattices analytically proves difficult [19,20], especially in the case of compact rings where the fringe fields and curvature play a significant role, leading to a closed orbit independent of the magnet geometry. The detailed transverse beam dynamics study thus requires numerical simulation codes that allow long-term particle tracking in 3D complex highly nonlinear magnetic fields, which are equipped with advanced analysis tools to consider linear and nonlinear coupling. The ZGOUBI ray-tracing code [21–23] is ideally suited for this purpose as it performs step-by-step particle tracking in complex, realistic magnetic field models and field maps, including the field nonlinearities, the fringe fields, and possible magnet misalignments [16]. It also offers the possibility to linearly superimpose 3D field maps to characterize the influence of neighboring cells on the lattice parameters. Tracking in field maps allows for using ZGOUBI for experimental validation at later stages of the study with measured magnetic field maps. In addition, ZGOUBIDOO [24]—a modern Python 3 interface for ZGOUBI—can perform advanced analyses of tracking results for linear and nonlinear beam dynamics studies [25]. Specifically, the generalized lattice functions from linear coupling parametrizations that we recently implemented in ZGOUBIDOO can be computed inside the vFFA elements, as described in Ref. [15].

This paper studies in detail the linear and nonlinear beam dynamics of the FETS-vFFA prototype with the vFFA elements field falloff modeled by an arctangent function. This vFFA prototype has been designed with codes dedicated to fixed-field accelerators (SCODE [26] and FIXFIELD [27]). Studying this lattice with ZGOUBI and ZGOUBIDOO allows for cross-validation of these design studies and for exploring this lattice beam dynamics with advanced analysis tools and methods. This detailed study includes a thorough analysis of the neighboring cell residual field influence, the investigation of the lattice linear coupling, and the characterization of the DA in the 4D phase space.

The structure of this paper is as follows. Section II describes the FETS-vFFA prototype lattice and the methods used in ZGOUBI to track particles in this lattice. Section III explores the linear beam dynamics of the lattice, from the search of closed orbits accounting for neighboring cell residual fields to the computation of the eigentunes and lattice functions with different coupling parametrizations. The linear beam dynamics results are compared with those obtained with other codes, validating the design studies of the lattice. Section IV studies in detail the nonlinear beam dynamics, including the characterization of the DA in terms of the stability domain volume and complexity, and the computation of the acceptance hypersphere. Finally, conclusions on this first detailed study of such strongly coupled and nonlinear lattice are provided in Sec. V.

II. LATTICE AND METHODS

A. The FETS-vFFA lattice

In this work, Y is the horizontal coordinate, Z is the vertical coordinate, and X is the longitudinal coordinate in the Cartesian frame, while (y, z, s) are the coordinates in the moving Frenet-Serret reference frame attached to the reference trajectory. The vFFA field components in the median plane—the vertical plane at $Y = 0$—are as follows:

$$B_Y(Y = 0, Z, X) = 0, \tag{1}$$

$$B_Z(Y=0,Z,X) = B_0 e^{kZ} g(X), \tag{2}$$

$$B_X(Y=0,Z,X) = \frac{B_0}{k} e^{kZ} \frac{dg}{dX}, \tag{3}$$

where $g(X)$ represents the fringe fields of the magnet and describes the longitudinal dependence of the field. The vFFA magnetic field can be expressed at any position (Y,Z,X), assuming $Z_0 = 0$, with an out-of-plane polynomial expansion of order N [8]:

$$B_Y(Y,Z,X) = B_0 e^{kZ} \sum_{i=0}^{N} b_{Yi}(X) Y^i, \tag{4}$$

$$B_Z(Y,Z,X) = B_0 e^{kZ} \sum_{i=0}^{N} b_{Zi}(X) Y^i, \tag{5}$$

$$B_X(Y,Z,X) = B_0 e^{kZ} \sum_{i=0}^{N} b_{Xi}(X) Y^i, \tag{6}$$

where the coefficients in these expressions are given by recurrence relations and ensure the magnetic field respects Maxwell's equations [8]:

$$b_{Y0}(X) = 0, \qquad b_{Y,i+1}(X) = -\frac{1}{i+1}\left(k b_{Zi} + \frac{db_{Xi}}{dX}\right),$$

$$b_{Z0}(X) = g(X), \qquad b_{Z,i+2}(X) = \frac{k}{i+2} b_{Y,i+1},$$

$$b_{X0}(X) = \frac{1}{k}\frac{dg}{dX}, \qquad b_{X,i+2}(X) = \frac{1}{i+2}\frac{db_{Y,i+1}}{dX}.$$

To compute the magnetic field outside the median plane, all the field maps used in this work contain magnetic fields computed with the series of Eqs. (4)–(6) truncated at the tenth order. This truncation order has been shown to be adequate in the case of hyperbolic tangent fringe field function, with a convergence of the eigentunes and transfer matrix coefficients from the tenth order onward [8,16].

The magnetic field of vFFAs can be modeled using various fringe field functions $g(X)$. Given the importance of fringe fields in the compact FETS-vFFA machine, it is essential to accurately model these fringe fields to allow for predicting experimental results with simulations. Although the hyperbolic tangent function is the most commonly used function to model vFFA fringe fields [4,8], and is, for example, used in the newly implemented ZGOUBI VFFA keyword [16], recent research has highlighted its limitations in accurately describing the fringe field falloff of realistic vFFA magnets [17]. The design of a realistic coil-dominated vFFA magnet prototype has been performed and has shown that an arctangent function better describes the vFFA magnetic fields, allowing for obtaining similar tunes and closed orbits to the ones obtained with the coil configuration field map generated with a 3D magnet computation code [17]. The fringe field function $g(X)$ of the FETS-vFFA prototype is thus currently modeled by an arctangent function:

$$g(X) = \left[\arctan\left(\frac{X}{h_g}\right) - \arctan\left(\frac{X - L_{\mathrm{mag}}}{h_g}\right)\right]/\pi, \tag{7}$$

where h_g represents the fringe field extent, and L_{mag} is the length of the magnet. The fringe fields at the magnet entrance and exit are supposed to be identical. The arctangent fringe fields drop slower to zero than the hyperbolic tangent fringe fields for an equivalent fringe field extent, as shown in Fig. 1. Hence, the residual fields are more significant at large distance, which results in a greater impact on the neighboring cells on the main cell closed orbit and optical parameters. Consequently, the methods used to study such lattices cannot assume that the closed orbit deviation due to these residual fields is negligible. It is necessary to superimpose field maps from neighboring cells in ZGOUBI to accurately account for the fringe field effects in this lattice.

The FETS-vFFA lattice is the 10-cell vFFA prototype lattice described in Ref. [14], designed to accelerate protons from 3 to 12 MeV. Most of the results presented in this work are obtained for the nominal energy of 3 MeV. Table I

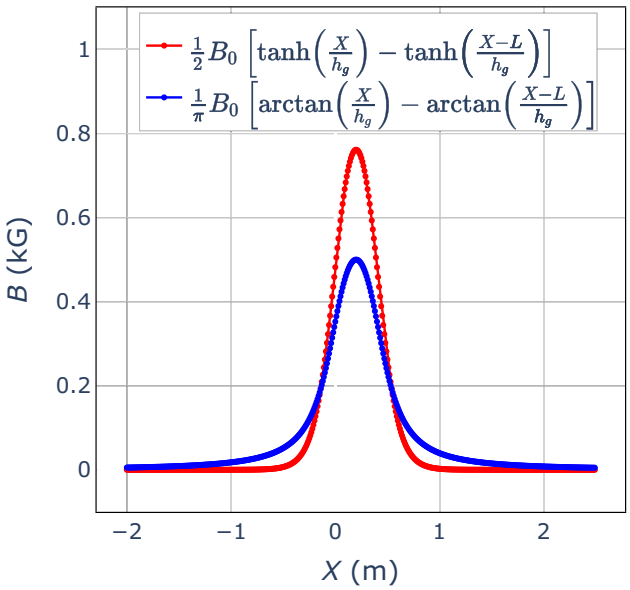

FIG. 1. Fringe field falloff modeled by the hyperbolic tangent and arctangent functions for $B_0 = 1.0$ kG, $h_g = 0.2$ m, and $L = 0.4$ m. The magnetic field is normalized so that both integrated fields are the same. The arctangent fringe fields drop slower to zero than the hyperbolic tangent fringe fields, leading to the necessary consideration of the neighboring cell residual fields. These large residual fields significantly impact the cell parameters and need to be accurately considered to obtain correct closed orbit and linear optics.

TABLE I. Design parameters of the FETS-vFFA prototype from Ref. [14].

Parameters	
Energy	3 to 12 MeV
Number of cells	10
Cell length	2.8 m
Bd magnet length	0.5 m
Bf magnet length	0.5 m
Straight length	1.24 m
Distance between Bd center and Bf center	0.53 m
Fringe field extent (h_g)	0.15 m
Bd/Bf ratio	1.15
Normalized field gradient (k)	1.31 m^{-1}

shows the main design parameters of the FETS-vFFA prototype with the vFFA elements field falloff modeled by an arctangent function, including the details of the periodic cell. A section of the 3D magnetic field map associated with this periodic cell is shown in Fig. 2, along with the periodic nominal energy orbit inside the cell. It is a focusing-defocusing-focusing (FDF) triplet lattice with the three vFFA magnets (Bf, Bd, and Bf magnets) aligned on a straight line. Each cell has a length of 2.8 m and a bending angle of 36°. The complete ring forms a polygon with each side consisting of a cell, as illustrated in Fig. 3. In addition to the strong focusing provided by the cell structure (radial focusing due to the sector-alternating field), the focusing is also influenced by the fringe fields and edge focusing as the particle does not enter the cell perpendicularly to the magnet faces.

Figure 4 shows the vertical particle trajectories found on a single cell for different energies, along with the magnetic field components along these trajectories. The orbits are stacked vertically on top of each other, and the magnetic

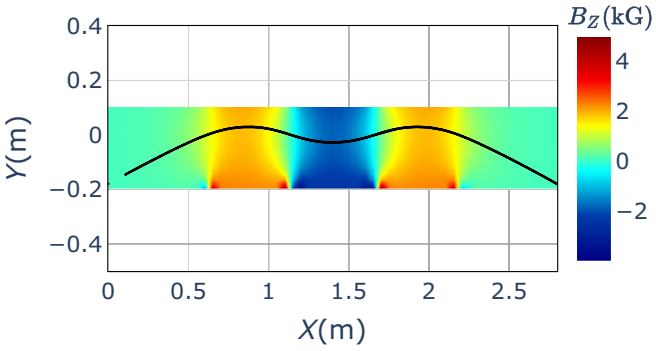

FIG. 2. Section of the 3D magnetic field map constructed with ZGOUBIDOO for one cell of the FETS-vFFA prototype. The field map shows the vertical component of the magnetic field. The cell comprises three magnets aligned on a straight line, with an FDF triplet focusing structure; the central magnet has a reverse bending field, while the two outer magnets have a normal bending field. The magnet normalized field gradient is 1.31 m^{-1}. The cell has a length of 2.8 m and a bending angle of 36°. The periodic nominal energy orbit inside the cell is shown in black.

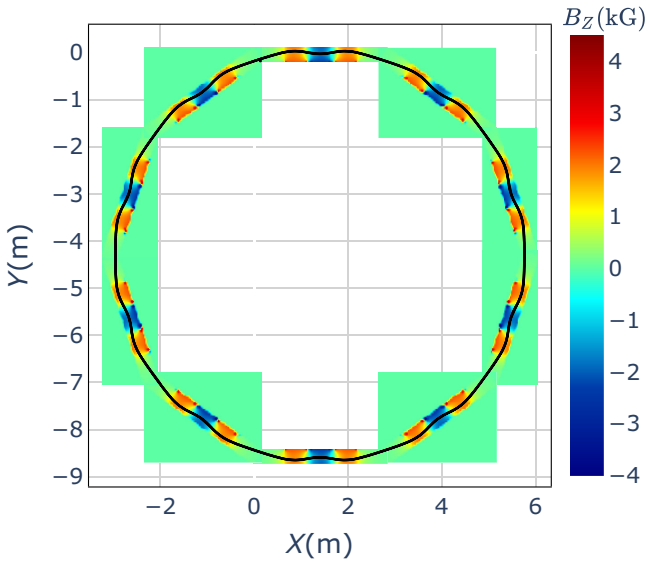

FIG. 3. Magnetic field map of the entire FETS-vFFA ring. The 3 MeV closed orbit is shown in black. The lattice consists of 10 FDF cells and is designed to accelerate protons from 3 to 12 MeV. The complete ring forms a polygon with each side consisting of a cell with a length of 2.8 m, a bending angle of 36°, and the three vFFA magnets aligned on a straight line.

field components scale with the particle energy, as expected in vFFAs. The vertical orbit excursion for the energy range 3–12 MeV corresponds to 53 cm, which is equivalent to the orbit excursion obtained using SCODE [14]. The significant residual fields (∼0.1 kG) remaining in all directions at the cell ends, as depicted in Fig. 5, show the necessity to consider the neighboring cell influence to study the closed orbit shape and transverse beam dynamics of this lattice accurately.

B. Tracking with ZGOUBI

As the residual fields are significant at the cell ends in the FETS-vFFA lattice and greatly impact the particle trajectory, it is crucial to superimpose the fields from neighboring elements. It can be achieved by superposing field maps using the TOSCA keyword in ZGOUBI [28]. Since the field maps of the FETS-vFFA cells are rectangular, it is important to define appropriate integration limits in order to integrate within polar sectors and prevent overlap between consecutive cells' field maps. This ensures trajectory continuity between neighboring cells, as detailed in Appendix.

III. LINEAR BEAM DYNAMICS

A. Closed orbit and eigentunes

The significant residual fields from neighboring cells, particularly the longitudinal field B_X, substantially impact the optical lattice parameters. Accurately determining the stable closed orbit and eigentunes requires proper field

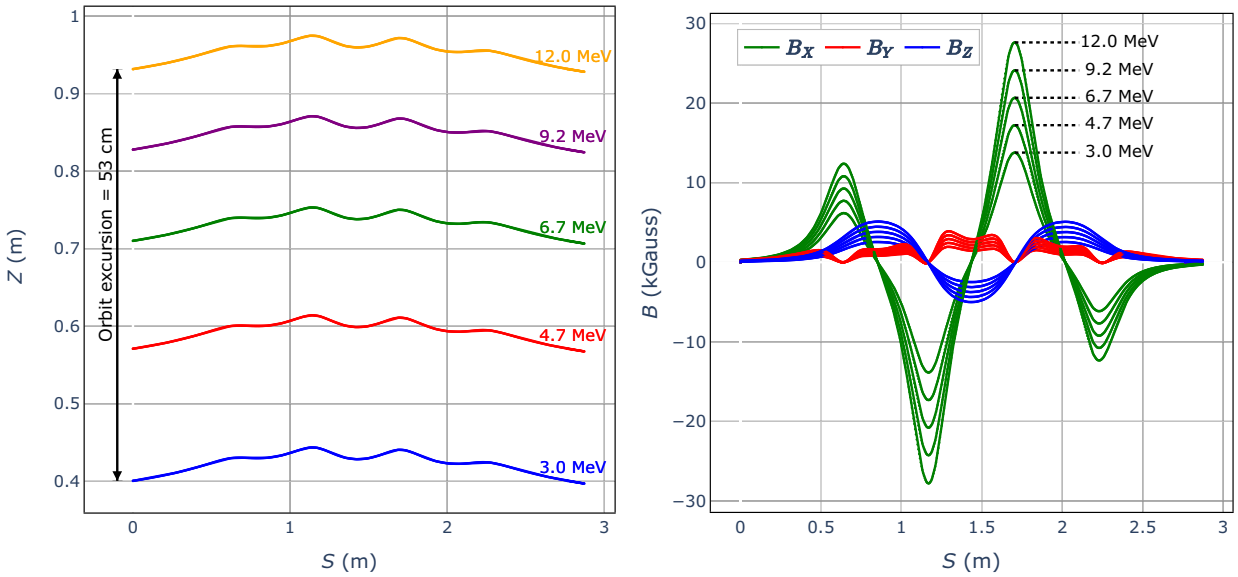

FIG. 4. Vertical particle trajectories and magnetic field components along these trajectories for energies ranging from 3 to 12 MeV. The vertical orbit excursion with energy is observable, as expected in vFFAs. The magnetic field scales with energy as all its components satisfy the exponential scaling condition. The particle trajectory is found on a single cell without considering the influence of neighboring cells. This single-cell trajectory does not correspond to the closed orbit as the vertical divergence does not cancel out at the cell ends. Finding an orbit satisfying the periodic conditions on all initial particle coordinates is not possible without considering neighboring cells.

modeling, including these residual fields. Appendix details the procedures for constructing field maps and considering different extents for neighboring cells. It further explores the linear beam dynamics of the lattice under varying influences from neighboring cells. The results reveal that additional residual fields significantly affect the closed orbit shape and eigentunes, impact the closed orbit vertical extension, and lead to a vertical orbit excursion. By adequately considering the residual fields, we obtained a closed orbit with zero vertical divergence at both ends, similar to the closed orbit obtained using SCODE during the design stage [14]. We also computed the cell eigentunes, which are the tunes of the linearly decoupled motions. These eigentunes correspond to the arguments of each conjugate pair of eigenvalues of the one-cell 4×4 periodic transfer matrix.[3] We obtained $(1-\nu_1, \nu_2) = (0.24362, 0.119732)$, which are similar to the eigentunes computed with SCODE (0.243445, 0.12002) [14]. One eigentune is larger than 0.5, indicating that the cell phase advance exceeds 180°. The differences in tunes between SCODE and ZGOUBI are smaller than 10^{-3}, which is acceptable as it can be explained by the influence of other simulation parameters (including the field map mesh size).

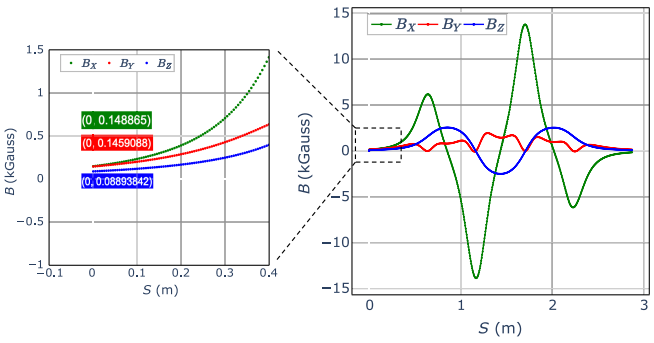

FIG. 5. Magnetic field components along the single-cell trajectory for a particle at 3 MeV. The residual fields at the cell ends are significant in all directions, leading to a great influence of the neighboring cells on the closed orbit and cell linear parameters.

B. Lattice functions with coupling parametrizations

Due to their magnetic field's longitudinal and skew quadrupolar components, vFFAs exhibit linear transverse motion coupling originating by design. The one-cell 4×4 periodic transfer matrix

$$\hat{\mathbf{M}} = \begin{pmatrix} \mathbf{A} & \mathbf{B} \\ \mathbf{C} & \mathbf{D} \end{pmatrix} \tag{8}$$

features nonzero off-diagonal elements; an adequate parametrization of the linear optics is required to explore their linear beam dynamics in detail. Two main parametrizations are generally put forth to describe the coupled optics: the parametrization of Edwards and Teng (ET) [29] and the one of Mais and Ripken (MR) [30]. The ET and MR

[3]The one-cell periodic transfer matrix is obtained by tracking several particles with small offsets from the reference particle in each direction.

parametrizations were extended and revisited in several works, and other variants can be linked to these two parametrization categories. An in-depth review of the coupled betatron motion parametrizations with their parameter interpretation can be found in Ref. [15].

The ET parametrization allows computing the linear invariants and studying the motion in the linearly decoupled planes, which is especially helpful when studying the DA. The ET generalized Twiss parameters describe the two oscillation eigenmodes in the decoupled space but are not easily interpretable in the coupled physical space. By contrast, the MR parametrization offers more interpretable lattice functions that can be linked to measurable beam parameters, such as beam sizes. These functions represent the effect of the two oscillation eigenmodes on each physical transverse direction, providing insight into the focusing properties of the lattice. A variant of the MR parametrization is the parametrization of Lebedev and Bogacz (LB) [31], which provides interesting additional parameters, including the parameter U that characterizes the coupling strength. This parameter is directly linked to the rotation angle of the decoupling matrix $\tilde{\mathbf{R}}$ in the ET parametrization.

Since the ET and MR parametrizations provide complementary information, it is essential to compute both sets of parameters. The ET and LB parametrizations have been implemented in ZGOUBIDOO [15]. With the ZGOUBI capabilities of step-by-step tracking inside the elements, ZGOUBIDOO can compute the transfer matrices and the ET and LB parameters at each integration step [25]. Figure 6 shows the β functions from the ET parametrization computed on one cell of the FETS-vFFA lattice. The significant difference between both β functions indicates that one of the cell phase advances is bigger than 180°. Figure 7 shows the β functions from the LB parametrization, indicating the evolution of the beam envelope in the laboratory axes along the lattice. The phase advances are shown in Fig. 8 and are identical for the ET and LB parametrizations.

In addition to the generalized Twiss parameters, the ET parametrization provides the decoupling matrix $\tilde{\mathbf{R}}$ that allows switching easily between the coupled and decoupled spaces. For the FETS-vFFA cell, the decoupling matrix is

$$\tilde{\mathbf{R}} = \begin{pmatrix} 1.04 & 0.0 & 0.203 & 0.0341 \\ 0.0 & 1.04 & -0.00523 & -0.396 \\ 0.390 & 0.0315 & 1.04 & 0.0 \\ -0.0675 & -0.201 & 0.0 & 1.04 \end{pmatrix}. \quad (9)$$

As highlighted in Ref. [15], only one solution exists for the decoupling matrix at specific locations of the lattice ($|\mathbf{B} + \bar{\mathbf{C}}| < 0$), forcing the mode identification. When the mode identification is incorrect, a "forced mode flip" occurs. The condition $|\mathbf{B} + \bar{\mathbf{C}}| < 0$ corresponds to

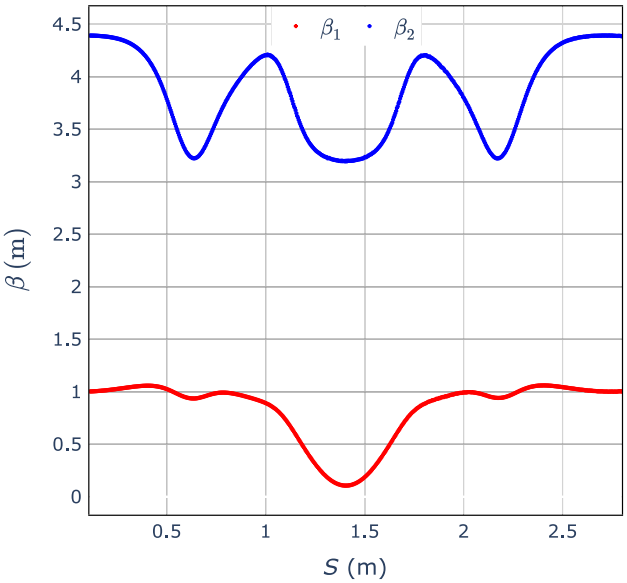

FIG. 6. β functions from the ET parametrization computed on one cell of the FETS-vFFA lattice. These lattice functions are used to compute the linear invariants of motion.

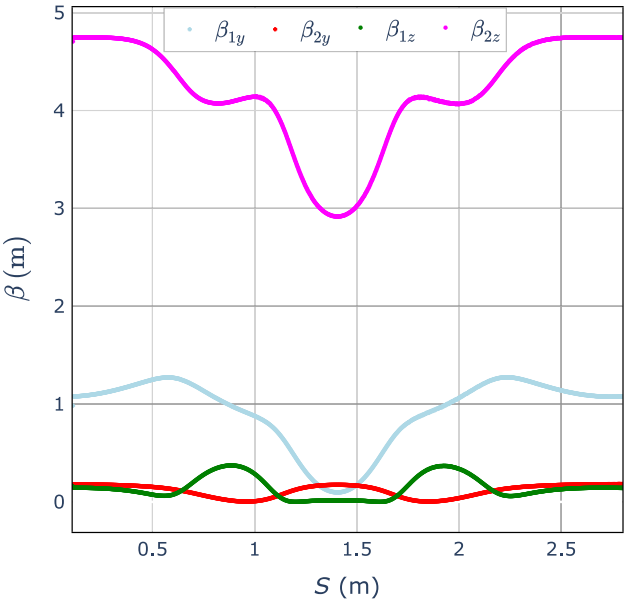

FIG. 7. β functions from the LB parametrization computed on one cell of the FETS-vFFA lattice. These lattice functions indicate the evolution of the beam envelope in the laboratory axes along the lattice.

$U < 0$ in the LB parametrization, as shown in Fig. 9(a). For the FETS-vFFA lattice, the parameter U was computed by imposing periodic conditions. This parameter is negative at some places of the cell, as shown in Fig. 9(a). It varies in sections where coupling fields are present and reflects how the section couples the motion compared to the average coupling in the cell. In the FETS-vFFA, a mix of skew quadrupoles and longitudinal field components impact the

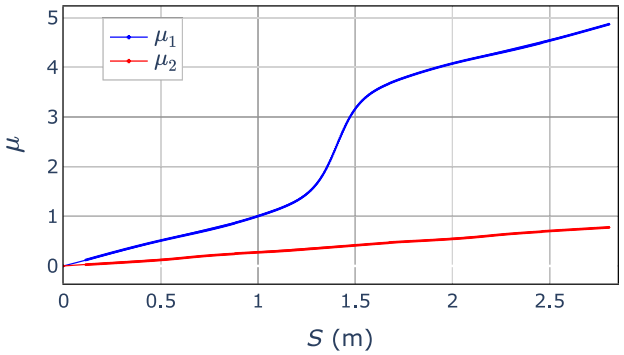

FIG. 8. Phase advances on one cell of the FETS-vFFA lattice. The phase advances obtained with the ET and LB parametrizations are the same by definition.

parameter U throughout the cell. The β functions of the ET parametrization computed on the FETS-vFFA cell by considering the wrong mode identification are shown in Fig. 9(b) and become infinite when $|\mathbf{B}+\bar{\mathbf{C}}|=0$, confirming that only one mode identification is correct in this case. The LB parametrization imposes $U<1$ so that the derivatives of the phase advances $d\mu_1/ds$ and $d\mu_2/ds$ are always positive (phase advances monotonously increasing). Finally, it is interesting to note that if the parameter U is negative, the corresponding ET rotation angle ϕ is complex. It corresponds to a rotation of the plane (u,p_u) compared to the plane (y,p_y).

To summarize, transverse betatron motion coupling is generally observed in lattices featuring separated solenoids and skew quadrupoles, which are the main sources of linear coupling. In vFFAs, principal focusing elements consist of longitudinal and skew quadrupolar components. Both coupling fields are present simultaneously, which lead to complex coupled linear optics; peculiar phenomena like forced mode flip appear more likely than in other types of accelerators. If the mode identification becomes incorrect throughout the lattice when forced mode flip conditions occur, the ET β functions can diverge completely and become infinite, as we have observed in Fig. 9(b). The ET and LB parametrizations, which we have computed, provide complementary information, with their respective generalized Twiss parameters serving different purposes. On the one hand, the ET lattice functions, including the β functions presented in Fig. 6, give information on the oscillation eigenmodes and are particularly useful for computing the linear invariants. Moreover, the decoupling matrix of Eq. (9) allows for studying the motion in the linearly decoupled planes. On the other hand, the LB lattice functions, including the β functions presented in Fig. 7, characterize the amplitude of the betatron oscillations and allow computing the beam sizes when invariants in the linearly decoupled planes are provided, as explained in detail in Sec. IV D.

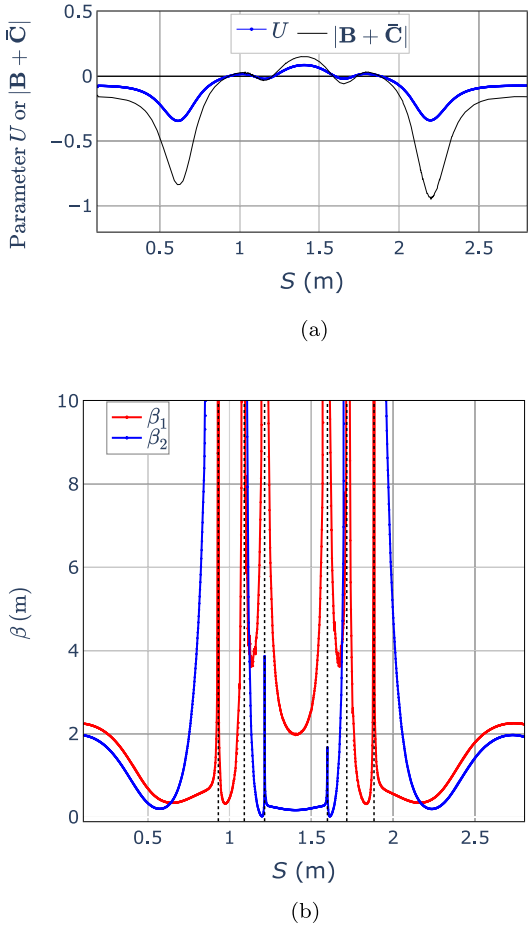

FIG. 9. Forced mode flip illustrated on the FETS-vFFA lattice. (a) Periodic U of the LB parametrization, and $|\mathbf{B}+\bar{\mathbf{C}}|$ of the one-cell periodic coupled transfer matrix $\hat{\mathbf{M}}$. The condition $|\mathbf{B}+\bar{\mathbf{C}}|<0$ reflects the existence of only one solution for the decoupling matrix and corresponds to a negative LB parameter U. This parameter varies all along the cell, indicating the influence of coupling fields throughout cell. When $U<0$, the ET rotation angle of the symplectic rotation matrix is complex, indicating an exchange between the position and momentum coordinates. (b) β-functions of the FETS-vFFA cell using the ET parametrization by imposing the wrong mode identification. The β-functions cannot be defined (or become infinite) when $|\mathbf{B}+\bar{\mathbf{C}}|=0$, indicated by the dashed black lines. In this case, only one solution for the decoupling matrix exists with only one mode identification.

IV. NONLINEAR BEAM DYNAMICS

A. Computation of the linear invariants in the linearly decoupled planes

To study the FETS-vFFA nonlinear beam dynamics, the normalized linear invariants in the decoupled phase spaces (u,p_u) and (v,p_v) were computed. To that end, we searched for the maximum amplitudes in the u and v directions (with $p_u=0$ and $p_v=0$) for which the particle survives 1000 turns. From the maximum amplitude particle

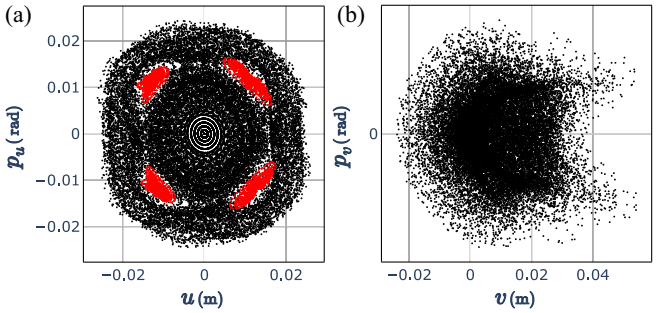

FIG. 10. Linearly decoupled phase spaces (u, p_u) and (v, p_v) obtained by tracking particles with several initial amplitudes in $[0, u_{\max}]$ (with $p_u = 0$) (a) and in $[0, v_{\max}]$ (with $p_v = 0$) (b) and sampling the particle's position at each turn. The linear invariants ($e_u = 43.47\ \pi$ mm mrad and $e_v = 41.21\ \pi$ mm mrad) are computed with the coordinates of the particles with the maximum amplitudes in the u and v directions ($u_{\max}, p_u = 0$ and $v_{\max}, p_v = 0$) and the ET lattice functions. Particles initially launched in the islands, represented by red points, remain in the islands and exhibit a fractional cell tune of 0.25.

coordinates in each linearly decoupled plane, the linear invariants e_u and e_v were computed with the Courant-Snyder formula $\gamma(s)y^2 + 2\alpha(s)yy' + \beta(s)y'^2 = \epsilon$ (where y represents both linearly decoupled coordinates) [32]. We obtained $e_u = 43.47\,\pi$mm mrad and $e_v = 41.21\,\pi$mm mrad. By tracking several particles with different initial amplitudes in the u and v directions, we observed the appearance of stability islands, corresponding to fixed points of the fourth order, as shown in Fig. 10. When particles are initially launched in the islands (red points in Fig. 10), they remain in the islands and exhibit a fractional cell tune of 0.25.

As vFFAs are strongly coupled and nonlinear machines, the study of their nonlinear beam dynamics must account for linear and nonlinear coupling. The particle motion explores the full 4D phase space, and particle oscillation amplitude exists in both linearly decoupled planes [33]:

$$u = r\cos(\alpha)\cos(\theta_1), \qquad p_u = r\cos(\alpha)\sin(\theta_1), \quad (10)$$

$$v = r\sin(\alpha)\cos(\theta_2), \qquad p_v = r\sin(\alpha)\sin(\theta_2), \quad (11)$$

where r is the amplitude in the 4D phase space, θ_1, θ_2 are the angles in each decoupled plane, and α characterizes the ratio between the amplitudes in both linearly decoupled planes [34]. The 4D motion is reflected in the 2D linearly decoupled subspaces as diffuse layers where stable and weakly chaotic motion coexist [34–36], as shown in Fig. 10, where a small stable inner core and a more diffuse region clearly appear. Particles can be transported between both linearly decoupled planes; a particle may be transported from the chaotic layer in one plane to a high-amplitude region in the other plane, potentially leading to beam losses.

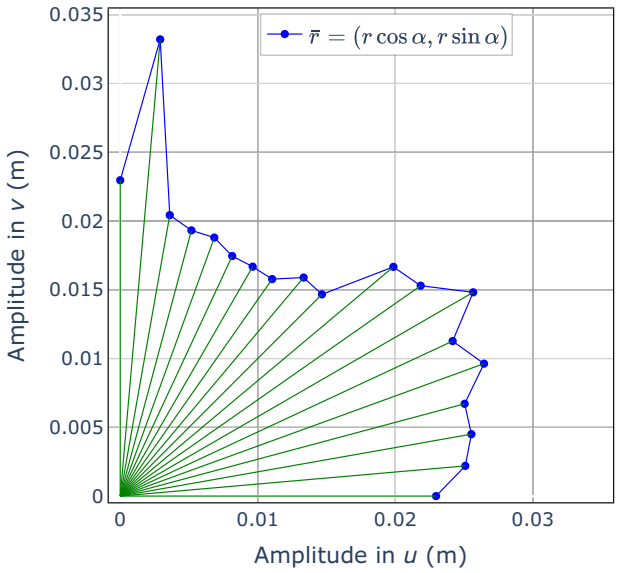

FIG. 11. Maximum amplitude in the 4D phase space for several α with $\theta_1 = \theta_2 = 0$. The maximum amplitude does depend on α because the machine is highly nonlinear, leading to an irregular phase space stability domain.

A first characterization of the lattice's nonlinear nature consists in computing the linear invariants for several ratios of amplitudes in both linearly decoupled planes. In the FETS-vFFA lattice, the maximum amplitude that survives 1000 turns is not constant with α, as shown in Fig. 11, highlighting the impact of nonlinearities on the phase space stability domain and the resulting phase space distortion. While this representation offers initial insights into the phase space distortion and nonlinear coupling, it should be interpreted with caution for lattices with high nonlinearity since it is based on linear optics, meaning that the linear invariants are computed assuming elliptical shapes in the 2D linearly decoupled phase spaces. This assumption is no longer valid when dealing with large nonlinearities. In this case, the proper distribution shape must be computed to obtain 2D invariants that can be related to the beam sizes in the coupled space using the LB lattice functions. Furthermore, these 2D invariants depend on the ratio of amplitudes in both linearly decoupled planes. Characterization of the stability domain in the full 4D phase space is thus required to capture the motion complexity and have a comprehensive understanding of beam dynamics and DA.

The DA is defined as the phase space region where the motion remains bounded for a given number of turns. In this work, we fully characterize the DA on 1000 turns, as it has been shown that the 2D DAs converge for 1000 turns on similar lattices [8]. When linear and nonlinear coupling occurs, the stability domain is a 4D volume without a well-defined boundary between stable and unstable motion [34,35]. To characterize the DA in highly nonlinear and strongly coupled machines, it is necessary to compute

TABLE II. Parameters and results for the methods to estimate the stability domain [18]. The 4D volumes are normalized by the relativistic factor $(\beta\gamma)^2$ and the equivalent radii are computed with these normalized volumes.

	Direct integration		
	(A) Scan over phase space variables	(B) Random sampling	(C) Integration over the dynamics
Description	(i) Create a mesh $(\alpha, \theta_1, \theta_2)$. (ii) For each $(\alpha, \theta_1, \theta_2)$, find the maximum radius particle that survives 1000 turns. (iii) Integrate over phase space variables with Eq. (12).	(i) Launch many particles with uniformly distributed coordinates. (ii) Keep the particles that survive 1000 turns. (iii) Divide the phase space into a mesh $(\alpha, \theta_1, \theta_2)$, with at least one initial coordinate in each bin. (iv) Retain the maximum amplitude particle for each bin and integrate with Eq. (12).	(i) Find the maximum radius for several α with $\bar{\theta}_1 = \bar{\theta}_2 = 0$. (ii) Track the particles with the maximum amplitudes and keep the 1000 iterations. (iii) Divide the phase space into a mesh with at least one iteration per bin. (iv) Compute the DA by averaging over the iterates.
Initial conditions	~3 million orbits scanned to find the maximum amplitude in $r = [0, 0.06]$ surviving 1000 turns for each point of the integration mesh. It gives 157 339 particles with maximum amplitude.	28 million initial conditions uniformly distributed in a 4D hypersphere with $r = 0.06$ m, resulting in 1 164 518 initial conditions stable on 1000 turns.	1800 orbits evaluated to find 90 particles with maximum amplitude that survives 1000 turns for each α in [0°, 90°] with $\theta_1 = \theta_2 = 0$.
Integration mesh	$(\Delta\alpha, \Delta\theta_1, \Delta\theta_2) = (5°, 4°, 4°)$	$(\Delta\alpha, \Delta\theta_1, \Delta\theta_2) = (9°, 8.4°, 8.4°)$	$(\Delta\alpha, \Delta\theta_1, \Delta\theta_2) = (10°, 30°, 30°)$
DA (volume)	1408.86 π^2 mm^2 mrad^2	3395.62 π^2 mm^2 mrad^2	1467.09 π^2 mm^2 mrad^2
DA (equivalent radius)	7.286 mm	9.078 mm	7.36 mm
Pros and cons	(i) Find simply connected stability domain. (ii) CPU-intensive. (iii) Excellent DA estimate.	(i) Outliers increase the volume. (ii) CPU-intensive. (iii) Poor DA estimate.	(i) Nonuniform phase distribution. (ii) Less computationally demanding. (iii) Good DA estimate.

not only a measure of this 4D stability domain but also the effective radius of the acceptance hypersphere of the machine to evaluate the machine's operating performance in the coupled physical space [18]. Furthermore, an evaluation of the quality of the stability domain is needed to assess the phase space topology and spectral behavior of stable initial conditions and identify possible limitations of the DA. We thoroughly investigated the DA of the FETS-vFFA prototype by computing 4D estimates of the stability domain volume, metrics for evaluating the stability domain quality, and the largest 4D hypersphere inscribed to the stability domain to obtain the effective acceptance radius [18].

B. Estimates of the 4D stability domain volume

To estimate the stability domain volume, we have used three methods: the two methods established in Refs. [33,34] and referred to as "Direct integration with scan over phase space variables" and "Integration over the dynamics" to obtain the volume of the connected stability domain, and a random sampling method to obtain the total stability domain including points that may be disconnected from the main stability zone [18]. These three methods are summarized in Table II, along with the resulting DA volume and equivalent radius for the FETS-vFFA lattice with arctangent magnetic fringe fields.

The phase space variable scan method and the random sampling method consist in scanning a large number of orbits (either by searching the maximum amplitude particle that survives 1000 turns for each $(\alpha, \theta_1, \theta_2)$ in the integration mesh or by randomly scanning the phase space and retaining the coordinate with the largest radius in each bin of the integration mesh), then performing a "direct integration" over the phase space variables [33]:

$$V = \frac{1}{8}\int_0^{2\pi}\int_0^{2\pi}\int_0^{\frac{\pi}{2}} [r(\alpha,\theta_1,\theta_2)]^4 \sin(2\alpha) d\alpha\, d\theta_1\, d\theta_2. \quad (12)$$

Each orbit evaluation requires a full ZGOUBI simulation that tracks the particle over 1000 turns. Tracking multiple particles on 1000 turns over a 28 m circumference ring with small integration steps for accurate tracking requires significant CPU resources and time. On the contrary, the

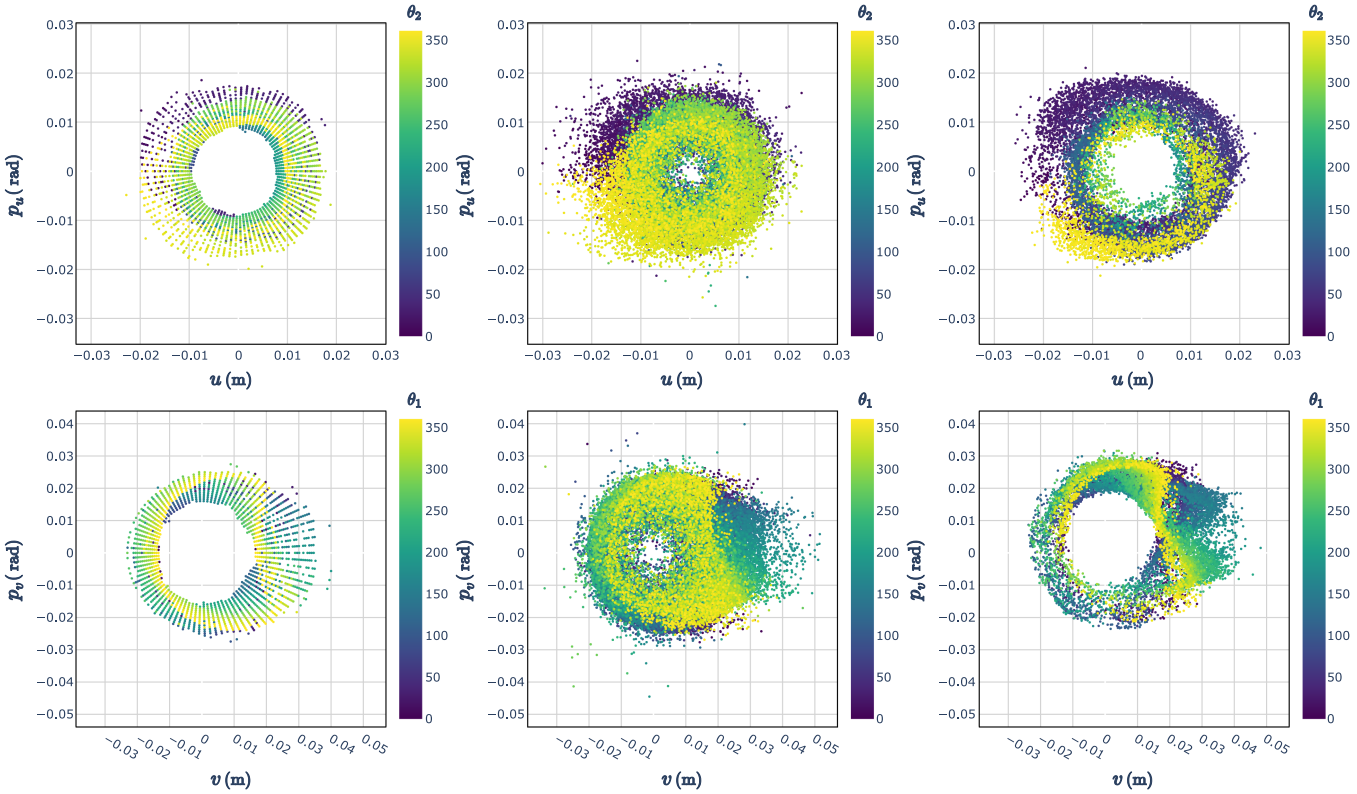

FIG. 12. Distributions of the surviving initial conditions for the scan and random sampling methods (left and center) and maximum amplitude particle iterates obtained with the integration over the dynamics method (right). All distributions are represented in the 2D linearly decoupled phase planes $(u - p_u)$ and $(v - p_v)$ for an amplitude ratio corresponding to $\alpha = 60° \pm 2.5°$. The outliers appearing in the random sampling distribution considerably increase the computed DA volume.

integration over the dynamics method allows for a reduction in CPU time by removing the scan over the phase plane angles θ_1 and θ_2. This method finds the particles with the maximum amplitudes for each α with fixed θ_1 and θ_2 and then performs an average over the iterations from the tracking of these maximum amplitude particles to compute the stability domain volume. As the phases of the iterations may not be uniformly distributed, this method requires dividing the angle space into a mesh that contains at least one initial condition per bin before performing the average [33,34].

Figure 12 shows the distributions of the surviving initial conditions for the scan and random sampling methods and the maximum amplitude particle iterates for the integration over the dynamics method. The distributions are represented in the 2D linearly decoupled phase planes $(u - p_u)$ and $(v - p_v)$ for an amplitude ratio corresponding to $\alpha = 60° \pm 2.5°$. The phase space variable scan method is the more reliable method and provides an accurate estimate of the volume of the simply connected stability domain; the random scanning method provides a poor DA estimate (relative error of 141% on the DA volume compared to the volume computed with the phase space variable scan method) as it retains stable outlier points in regions disconnected from the main stability domain. Figure 13 compares the stable initial condition distributions obtained with the scan and random sampling methods in the linearly decoupled planes for all α. It clearly highlights that both DA volumes differ from the outlier points. The integration over the dynamics method provides a suitable DA estimate (relative error of 4.13% on the DA volume compared to the estimate obtained with the phase space variable scan method) while saving considerable CPU time, as already observed in [18].

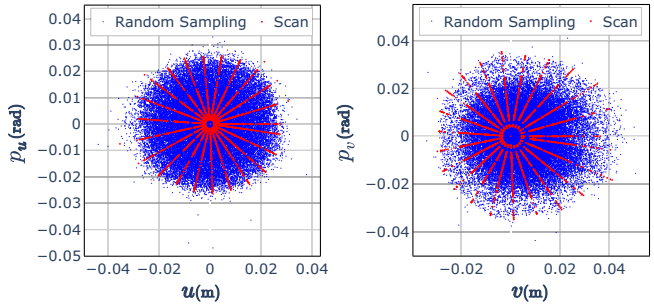

FIG. 13. Comparison of the stable initial condition distributions obtained with the scan and random sampling methods in the linearly decoupled planes for all α. The distributions are similar except for the outlier points at large amplitude, which leads to an increased DA volume for the random sampling method.

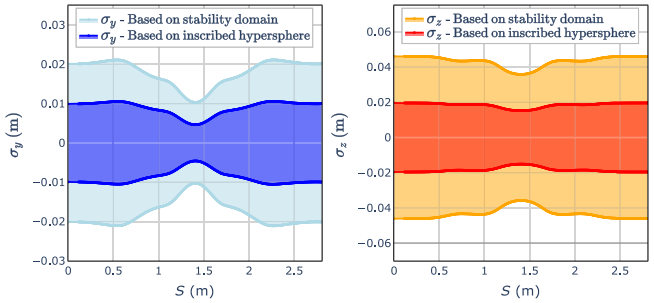

FIG. 14. Beam sizes (σ_y, σ_z) along the FETS-vFFA cell by defining the normalized 2D DAs with the area of the stable initial condition distributions for all α or with the acceptance hypersphere distributions in the linearly decoupled planes.

The 4D volumes computed with the three methods include the fourth-order stability islands; the initial conditions sampled in the islands result in bounded motion over 1000 turns even if they present a different dynamic. Detecting these stability islands can be achieved with detailed frequency analysis, as explained in Sec. IV E.

C. Practical definition of the DA in the coupled physical space

Due to the lattice nonlinearity, the stability domain can deviate significantly from a hypersphere. To obtain the effective radius of the acceptance hypersphere, corresponding to the maximal DA that ensures all particles injected in the coupled space survive 1000 turns, we have developed a method to determine the maximum hypersphere inscribed into the stability domain [18]. This DA definition has a more practical interpretable meaning as it can be directly linked to the beam injection into the machine if proper matching sections are designed. The radius of the maximum inscribed hypersphere centered on the closed orbit is 15.3 mm, which corresponds to a normalized volume of 175.48 π^2 mm^2 mrad^2, and a corresponding normalized radius $r = 4.328$ mm. It is significantly lower than the stability domain volume and equivalent radius (volume corresponding to 12.46% of the 4D stability domain volume).

As the stability domain center is slightly shifted from the closed orbit, especially in the v plane (see Fig. 13), the largest hypersphere that completely enters into the stability domain is also off-centered from the closed orbit. This off-centered hypersphere has a normalized volume of 258.58 π^2 mm^2 mrad^2 corresponding to an effective radius of 4.769 mm. This volume is slightly larger than the volume of the centered hypersphere. It corresponds to 18.35% of the stability domain volume, indicating that the phase space is significantly distorted due to vFFA nonlinearities. In practical applications, the DA can further be limited by magnet design and collimation system as the closed orbit may not align with the magnet centers.

D. Normalized 2D DAs and beam sizes

To compute the horizontal and vertical beam sizes using the LB parametrization, it is necessary to have normalized 2D DAs in linearly decoupled planes ε_I, ε_{II}:

$$\sigma_y = \sqrt{\beta_{1y}\varepsilon_I + \beta_{2y}\varepsilon_{II}}, \tag{13}$$

$$\sigma_z = \sqrt{\beta_{1z}\varepsilon_I + \beta_{2z}\varepsilon_{II}}. \tag{14}$$

A first approach defines these 2D DAs as the area of the stable initial condition distributions in the 2D linearly decoupled planes for all α (see Fig. 13). In this case, the 2D DAs are, respectively, 72.04 and 104.53 π mm mrad. Assuming a beam core emittance of one-third of the normalized DA (24.01 and 34.84 π mm mrad), the maximum beam sizes are 21.13 and 46.09 mm, as shown in Fig. 14. As vFFAs nonlinearities lead to significant phase space distortions, a second approach defines the normalized 2D DAs based on the acceptance hypersphere. The normalized DAs are then equal in both linearly decoupled planes and are 18.73 π mm mrad, leading to significantly reduced beam sizes ($\sigma_y = 10.54$ mm and $\sigma_z = 19.6$ mm). The values of 2D DAs, beam core, and beam sizes are summarized in Table III for both approaches.

TABLE III. 2D normalized DAs, beam core emittances, and beam sizes computed either with the distributions of stable initial conditions for all α or with the acceptance hypersphere distribution in the linearly decoupled planes.

	Stable initial conditions distribution in (u, p_u) and (v, p_v)	Acceptance hypersphere distribution in (u, p_u) and (v, p_v)
Normalized 2D DAs (π mm mrad)	(72.04, 104.53)	(18.73, 18.73)
Normalized beam core (π mm mrad)	(24.01, 33.83)	(6.24, 6.24)
Unnormalized beam core (π mm mrad)	(301.97, 438.16)	(78.51, 78.51)
β functions	$\beta_{1y,\max} = 1.27$ m $\beta_{2y,\max} = 0.18$ m, $\beta_{1z,\max} = 0.37$ m $\beta_{2z,\max} = 4.75$ m	
Beam size in y (mm)	21.13	10.54
Beam size in z (mm)	46.09	19.6

TABLE IV. Metrics and analysis tools to characterize the complexity of the phase space stability domain.

	Frequency analysis		
	Main frequencies and nonlinearities	Diffusion coefficient and FMA	Clustering metric
Goals	(i) Detection of stability islands.	(i) Characterization of the system global dynamics.	(i) Characterization of the phase space distribution with different dynamics zones.
	(ii) Characterization of the lattice nonlinearity.	(ii) Identification of harmful resonances.	
Description	(i) Compute the frequency spectrum for each stable particle and detect stability islands from the main frequency histograms.	(i) Compute the diffusion coefficient for each point: $D = \log_{10}(\sqrt{(\Delta Q_u^2 + \Delta Q_v^2)})$ [37], where ΔQ_u and ΔQ_v are the eigentunes difference on the turn data halves.	(i) Use the scikit-learn DBSCAN function [38] to divide the points into clusters of similar density and noise.
	(ii) The metrics f_u and f_v are the medians of the frequency amplitude ratio distributions.	(ii) Analyze the tune diffusion map.	(ii) Compute the metric $h = \frac{\text{number of points in clusters}}{\text{total number of points}}$.
			(iii) Use the clustering to better visualize the different dynamics zones.
Results	(i) Fourth-order stability islands.	(i) Resonances: $-2\nu_1 + 3\nu_2 = 2$, $2\nu_1 + 5\nu_2 = 4$, and $2\nu_1 + \nu_2 = 1$.	(i) Island characteristic zones and separation between stable inner core and chaotic layer.
	(ii) $f_u = 0.627$, $f_v = 0.625$.		(ii) $h_u = 0.842$, $h_v = 0.84$.
Observations	(i) Only characterizes the u or the v motion at a time.	(i) Many particles inside the stability domain have slightly chaotic dynamics.	(i) The outliers influence the initial parameters.
	(ii) Complex dynamics underlying the importance of vFFA nonlinearities and nonlinear coupling.	(ii) High-order resonances impacting the DA.	(ii) Depends on the number of stable particles.
			(iii) Qualitative analysis tool that allows better visualization.

E. DA quality factors characterizing the complexity of the phase space stability domain

To have a more in-depth understanding of the nonlinear beam dynamics, we have used different analysis tools, such as detailed frequency analysis and clustering methods to highlight regions with different dynamics (such as stability islands). These analysis tools and corresponding metrics [18] are summarized in Table IV. They allow for rationalizing the relevant information contained within the phase space.

The first step to evaluate the phase space complexity is determining whether stability islands exist within the stability domain. In Fig. 10, we have observed the appearance of fourth-order stability islands by tracking several particles with different initial amplitudes in the u direction ($p_u = 0$, $v = 0$). These stability islands are manifested by characteristic holes in the iterates distribution. These "holes" are characterized by a reduced density in the phase space. They can be highlighted using a clustering method as illustrated in Fig. 15. The clustering

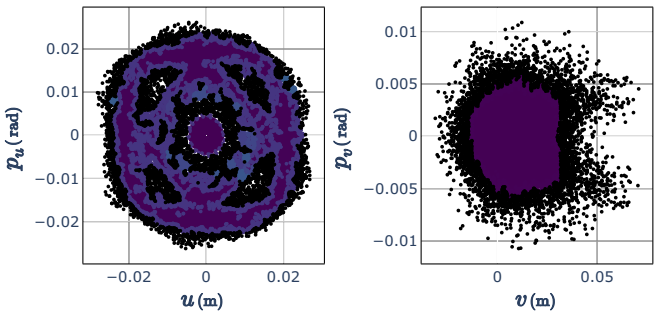

FIG. 15. The clustering method applied to the distribution of the iterates obtained with the tracking of 30 particles launched for $\theta_1 = 0$ and $\alpha = 0$ in the FETS-vFFA lattice. The clustering method is applied to 2D coordinates in the linearly decoupled phase planes. The characteristic holes from the fourth-order stability islands are highlighted, as well as the zone that separates the phase space macroscopic regions with different dynamics (small stable inner core and weakly chaotic layer).

also highlights the zone that separates the stable inner core and the diffuse weakly chaotic region.

While the distribution of iterates may exhibit characteristic island holes, the distribution of the stable initial conditions in the stability domain will not; the direct integration methods scan the entire phase space, such that initial conditions are launched within the stability islands and remain inside these islands. The DA volume estimates thus include the stability islands, and a frequency analysis method is necessary to distinguish the initial conditions within the islands from their main frequencies. To that end, we computed the frequency spectrum for each stable initial condition by performing a turn-by-turn frequency analysis of the particle motions in the u and v directions on 1024 cells with pyNAFF [39]—a Python library that implements the NAFF algorithm [40]. The presence of stability islands in the stability domain is detected by analyzing the histograms of the main frequencies of stable particles, shown in Fig. 16. A peak at the 0.25 frequency appears and indicates that 16.8% of particles are inside the islands.

We have evaluated the dynamics complexity of the particles whose main frequencies are close to the design tunes but outside of the stability islands by computing the ratio between the amplitude of the main peak in their frequency spectrum and the total amplitude in the spectrum. It provides indications on the nonlinear nature of the lattice. A small ratio indicates chaotic behavior with

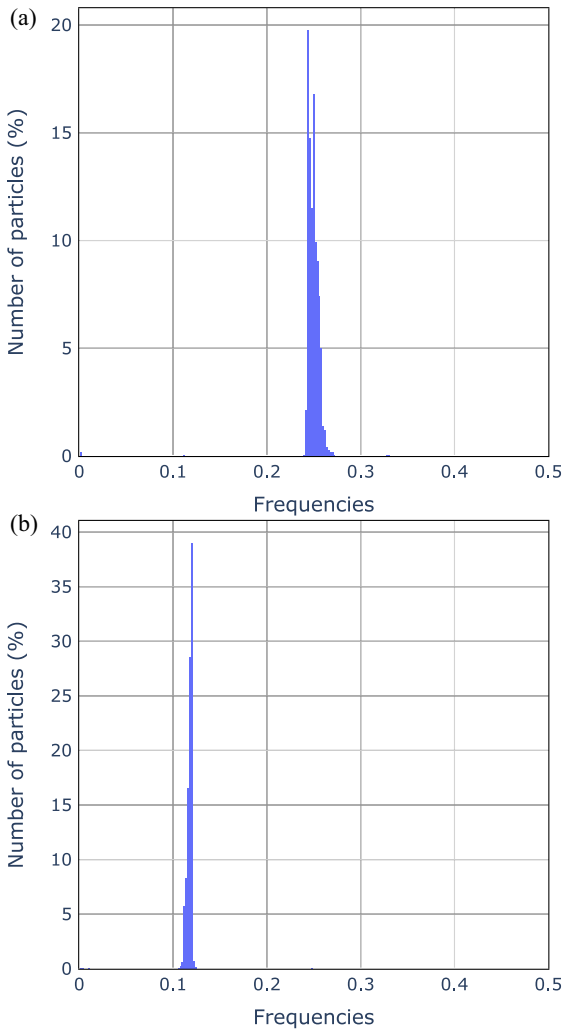

FIG. 16. Histograms of the main frequencies of all stable initial conditions. The main frequencies are retrieved for the motion in the u direction (a) and v direction (b). The main peaks correspond to the machine cell tunes, while the peak at the frequency 0.25 indicates the presence of fourth-order stability islands in the stability domain. The detuning with the amplitude is visible as the main peaks have finite widths.

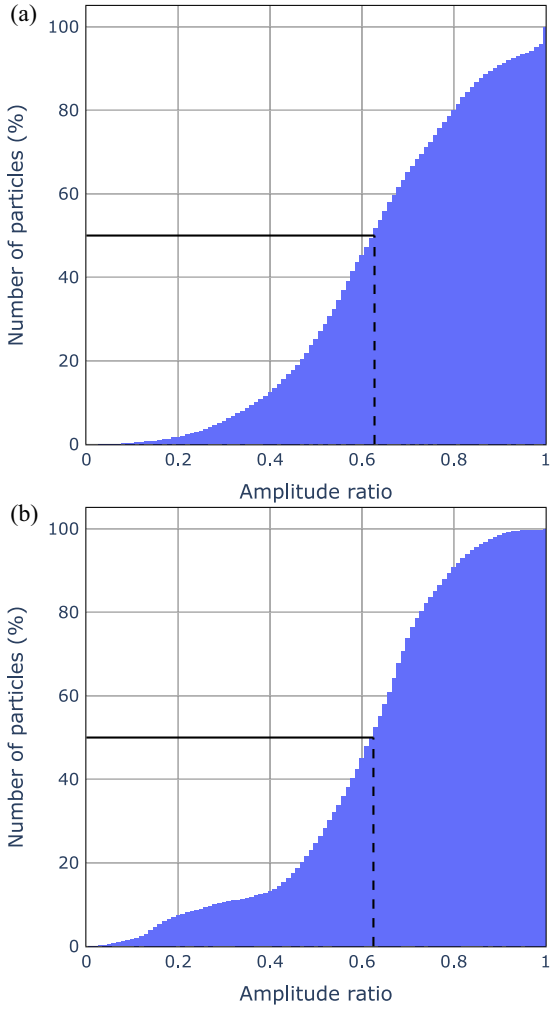

FIG. 17. Cumulative histograms of the ratio between the amplitude in the main peak and the total amplitude in the spectrum for each particle whose main frequencies are close to the machine cell tunes and do not stand in stability islands. These histograms correspond to the motion in the u direction (a) and the v direction (b). The medians are $f_u = 0.627$ and $f_v = 0.625$, indicating that many particles exhibit very complex dynamics with significant secondary peaks.

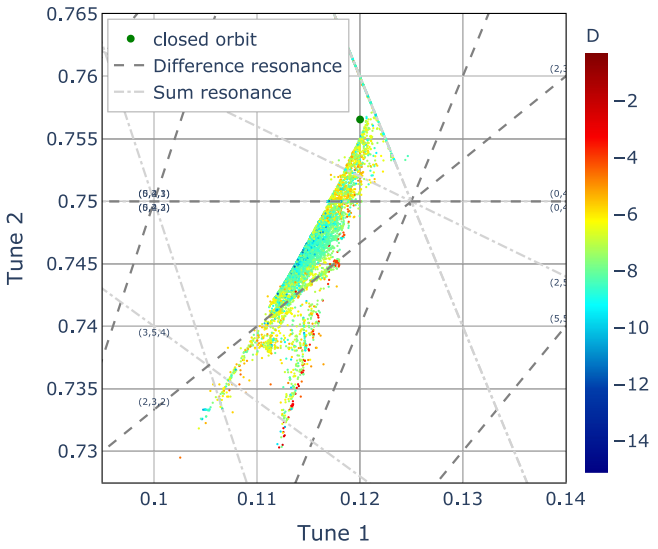

FIG. 18. Stable initial conditions for the random sampling method in the tune space with the points colored with their diffusion coefficient. The DA seems to be affected by the difference resonance $-2\nu_1 + 3\nu_2 = 2$ and by the sum resonances $2\nu_1 + 5\nu_2 = 4$ and $2\nu_1 + \nu_2 = 1$.

numerous significant secondary peaks, while a ratio of one indicates a linear motion with a single peak at the machine cell tune. The cumulative histograms of the frequency spectrum amplitude ratios for the u and v motions in the FETS-vFFA lattice, shown in Fig. 17, reveal a complex dynamics, which is significantly impacted by nonlinearities. Many particles have a very small amplitude ratio (the medians of the distributions are close to 0.6), indicating the presence of multiple secondary peaks in their frequency spectrum and the predominant role of nonlinear coupling.

Finally, we performed a frequency map analysis (FMA) [41,42] to gain insight into the phase space structure and highlight the resonances that could limit the DA, and hence, the performance of the machine. We have computed the diffusion of tunes on 1024 cells for each stable initial condition in the stability domain to better understand the global dynamics of the system. The tune diffusion map, shown in Fig. 18, indicates that the resonances that might affect the DA are the difference resonance $-2\nu_1 + 3\nu_2 = 2$ and the sum resonances $2\nu_1 + 5\nu_2 = 4$ and $2\nu_1 + \nu_2 = 1$. As already pointed out in [18], the importance of high-order resonances in vFFAs is not yet fully understood. Further studies are needed to mitigate them and increase the DA of such lattices. Finally, the tune diffusion map indicates that the tunes cross the resonance $4\nu_2 = 3$, which corresponds to the fourth-order stability islands and does not affect the particle motion.

V. SUMMARY AND CONCLUSIONS

We performed a detailed study of the FETS-vFFA prototype ring designed under the ISIS-II proton driver prototype project to accelerate proton beams from 3 to 12 MeV. To the best of our knowledge, this is the first comprehensive analysis of such a strongly coupled and highly nonlinear machine. Linear coupling that arises from the longitudinal and skew quadrupolar field components requires appropriate parametrization to study the linear beam dynamics, while nonlinear coupling requires studying the DA in the 4D phase space. In the FETS-vFFA compact ring, the fringe fields significantly impact the linear and nonlinear beam dynamics. We used the arctangent function to model the fringe fields of the vFFA magnets realistically, allowing for accurate validation against future experimental results. To accurately account for the significant influence of neighboring cells, we have superimposed the fields from neighboring elements by superposing field maps with ZGOUBI.

We explored linear beam dynamics and observed that the neighboring cell fields significantly affect the cell closed orbit and eigentunes. No closed orbit and stable optics can be found without accounting for these residual fields. The linear optics results found with ZGOUBI show excellent agreement with results from previous design studies obtained with SCODE. We investigated the FETS-vFFA linear optics with the two principal coupled betatron motion parametrizations (ET and MR). A thorough analysis of the ET decoupling matrix and LB parameter U revealed the occurrence of forced mode flip conditions (only one mode identification) when $U < 0$, leading to locally undefined or infinite ET β functions. On the one hand, the ET lattice functions were used to compute the linear invariants in the linearly decoupled planes ($e_u = 43.47\ \pi$ mm mrad and $e_v = 41.21\ \pi$ mm mrad). On the other hand, the LB lattice functions were used to compute the horizontal and vertical beam sizes. Specifically, we obtained $\sigma_y = 21.1$ mm and $\sigma_z = 46$ mm by defining the 2D DAs based on the stability domain distribution in the linearly decoupled planes, and $\sigma_y = 10.5$ mm and $\sigma_z = 19.6$ mm using the acceptance hypersphere instead.

We estimated the 4D stability domain volume to be 1408.86 π^2 mm^2 mrad^2, and the volume of the acceptance hypersphere to be 258.58 π^2 mm^2 mrad^2. The large difference in volumes shows the substantial phase space distortion resulting from vFFA nonlinearities. This phase space distortion results in a significant reduction of the achievable beam sizes when injecting an ellipsoidal bunch into the machine. From a practical perspective, defining the DA in terms of the acceptance hypersphere is more intuitive and easier to operate because it represents the volume of an ellipsoidal bunch that could remain stable during acceleration. Nevertheless, computing this acceptance hypersphere necessitates the knowledge of the 4D stability domain's delimitations, requiring more computational resources than determining the stability domain volume with fast integration over the dynamics method.

In addition to deforming the stability domain, vFFA nonlinearities also give rise to more complex particle dynamics within this stability domain, which has been highlighted by in-depth frequency analysis. The main frequency histograms revealed the presence of fourth-order stability islands, while the frequency spectrum amplitude ratio distributions emphasized that many particles have intricate frequency spectra with numerous significant secondary peaks. Finally, using the FMA method, we identified the difference resonance $-2\nu_1 + 3\nu_2 = 2$ and the sum resonances $2\nu_1 + 5\nu_2 = 4$ and $2\nu_1 + \nu_2 = 1$ as the high-order resonances that might limit the DA. Further studies are needed to better understand and mitigate these resonances and thus improve the performance of vFFA lattices. The simulation codes and advanced analysis tools used in this detailed study can be applied to completely model and analyze arbitrary vFFA lattices, from design studies to field map-based simulations with realistic fields. This paves the way for further experimental validation with 3D field maps, including possible magnetic field errors.

ACKNOWLEDGMENTS

The authors would like to thank D. Kelliher, J.-B. Lagrange, and S. Machida for the careful reading of the manuscript and insightful comments as well as for the many fruitful discussions. Marion Vanwelde is a research fellow of the Fonds de la Recherche Scientifique—FNRS.

APPENDIX: STUDY OF THE LINEAR OPTICS CONVERGENCE WITH THE NEIGHBORING CELL RESIDUAL FIELDS

Several methods exist in ZGOUBI to account for the possible influence of neighboring cells. The method generally used when working with ZGOUBI Cartesian elements—rectangular elements in ZGOUBI defined in local Cartesian coordinates—involves defining an integration zone greater than the cell extents to linearly superpose the neighboring cell residual fields [16,28]. By increasing the integration limits, ZGOUBI tracks the particles twice in the same spatial area, resulting in the superposition at the first order of the fields seen by the particle in neighboring elements, as illustrated in Fig. 19. This method is performed using the ZGOUBI parameters XE and XS for the Cartesian analytical model elements or by explicitly adding negative drifts at both cell ends and increasing field map extents in the case of field map elements. In both cases, the method is valid only for sufficiently small residual fields to ensure that the particle trajectory deviation due to these residual fields is limited. This is not the case in the arctangent FETS-vFFA lattice where residual fields are significant at the cell ends and greatly impact the particle trajectory. The only way to consider the neighboring cell influence accurately is to perform a proper superposition of neighboring fields. As obtaining this neighboring field

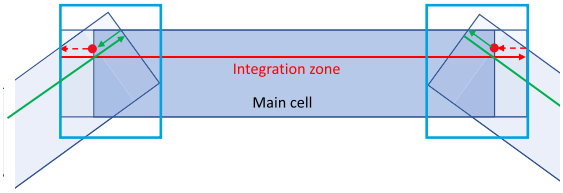

FIG. 19. Illustration of the commonly employed method to account for the influence of neighboring cells when working with Cartesian elements in ZGOUBI. The integration zone is extended, so that the field maps overlap. For the same region (blue boxes), ZGOUBI integrates inside the main cell and the neighboring element, hence superposing the fields seen by the particle in these neighboring elements. This method is only valid if the residual fields are small enough to ensure that the particle trajectory deviation due to these residual fields is limited, which is not the case in the arctangent FETS-vFFA lattice.

superposition with ZGOUBI analytical model elements proves difficult, all the following results use explicit field maps. We overlaid neighboring cell field maps in ZGOUBI, which is equivalent to tracking in a field map where the magnetic fields from neighboring elements are added.

1. Field maps construction

To build the field map of a single cell, we used ZGOUBIDOO together with an external code using the Python library Sympy [43] that allows for obtaining the analytical expressions of the vFFA magnetic field with the arctangent fringe fields. Since each cell of the ring is defined as rectangular patches defined in Cartesian coordinates, a frame rotation is necessary between the cells to account for the particle rotation and correctly place the element in the global reference frame. ZGOUBI can superimpose field maps with the "MOD" option of the TOSCA keyword, if these field maps have the same meshes [28]. The field maps of the rotated neighboring cells must thus have the same mesh as the main cell field map. Two methods, which will be discussed in detail subsequently, can be used to construct the field maps of the neighboring cells: one method involves particle tracking in ZGOUBI to construct field maps with finite extents from numerical simulations, while the other derives the analytical expressions of the rotated neighboring cell fields before creating the field maps. The former method creates field maps with explicit borders, while the latter provides the analytical expressions of the rotated fields for all points of the main cell mesh and hence is not limited by borders. Using and comparing both methods allow for validating them and studying the convergence of the cell linear parameters with the neighboring cell field map extension.

The first method ("numerical method"), which uses particle tracking in ZGOUBI, is illustrated in Fig. 20. The method consists in tracking particles of high rigidity (one particle per point in the transverse mesh) in a lattice composed of a drift and the rotated neighboring cell field

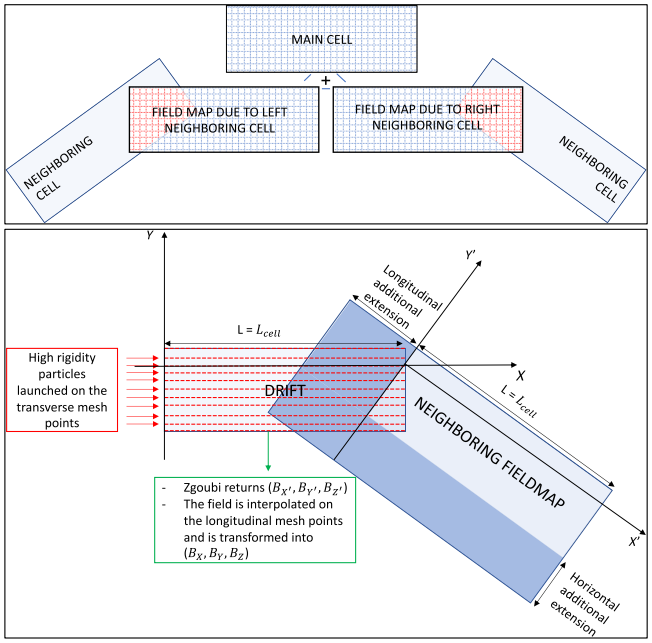

FIG. 20. Illustration of the method that uses particle tracking in ZGOUBI to construct the neighboring cell field maps with the main cell mesh. This method allows for constructing truncated field maps with finite longitudinal and horizontal extents to observe the influence of these extents on the optical parameters of the main cell. This method is CPU-intensive and produces coarse mesh field maps but is useful to perform convergence studies of the closed orbit and eigentunes with the increasing influence of the neighboring cells. The convergence should be obtained for neighboring field maps covering the entire orbit region.

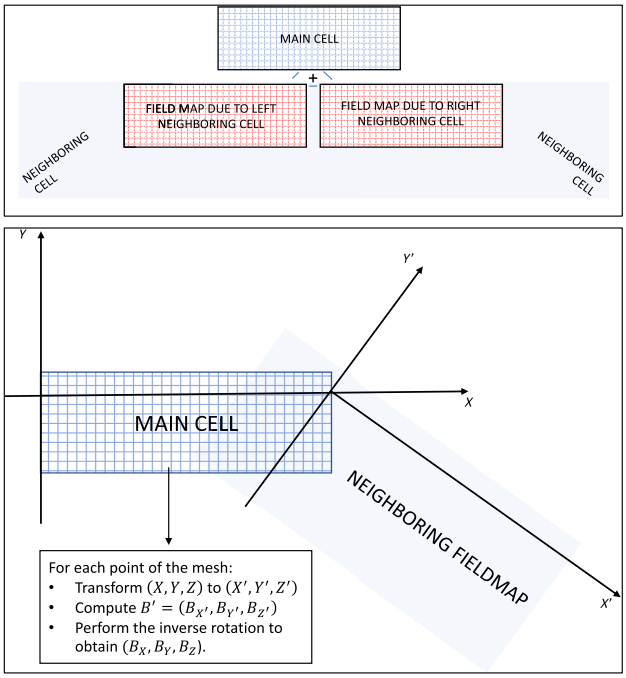

FIG. 21. Illustration of the method that uses the analytical expressions of the rotated neighboring fields to construct the neighboring cell field maps in the correct mesh. The resulting neighboring field maps cover the entire closed orbit region, leading to robust optics results. This method can produce field maps with arbitrary mesh sizes without too much increasing the computational resources.

map with finite longitudinal and horizontal extensions.[4] The explicit borders of the neighboring cell field maps lead to a variation of the residual fields taken into account with the extension of these field maps. The high-rigidity particles are not impacted by the magnetic field and follow a straight trajectory in the lattice. ZGOUBI then provides the magnetic field components along these straight trajectories in the particle reference frame. Due to the rotation between consecutive elements, a rotation must be applied to the field components to obtain the fields in the main cell reference frame. The field maps of the neighboring cells can then be created by correctly interpolating the field on the longitudinal mesh.

The second method ("analytical method"), which is based on analytical field expressions, is illustrated in Fig. 21. It consists in deriving the rotated fields' analytical expressions for the neighboring cells and performing several reference changes for the coordinates and fields. The neighboring field maps computed in this way automatically cover the entire closed orbit region, as the neighboring fields are obtained for each point of the mesh. It gives the most robust results as there is no more influence of the field map extents on the cell optics.

The numerical method requires considerable time and resources to have a fine mesh, as each transverse mesh point requires tracking one particle. On the contrary, the analytical method produces a field map with arbitrary mesh size without particle tracking. While the analytical method is the more robust method, the numerical method highlights the convergence of the cell optics results toward those obtained with the analytical method, thus validating both methods. Figure 22 compares the field components obtained with the analytical and numerical methods for different neighboring field map horizontal extensions. The magnetic fields from both methods are similar except for the field truncation in the numerical method due to the finite field map extents. Both methods should give the same results for numerical field maps with extents large enough to cover the entire closed orbit in the main cell.

Figure 23 shows the field components for the main cell and the neighboring cells. All field maps have the same mesh, allowing their superposition with the adequate ZGOUBI option (TOSCA keyword with MOD = 15 and MOD2 = 3 [28]). The additional fields due to the neighboring cells are significant, leading to a significant

[4]In order to have well-defined field map edges, we have artificially imposed that the magnetic field is zero outside the rotated field map, preventing the extrapolation performed by ZGOUBI for the points outside the field map mesh.

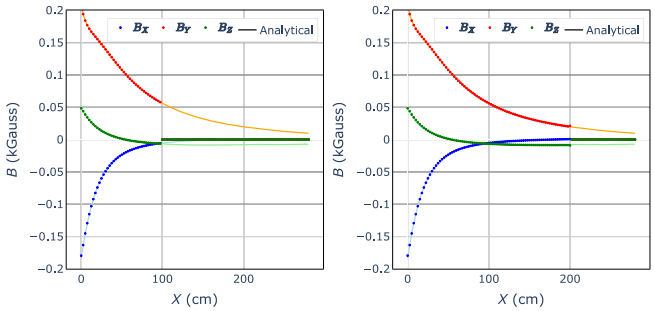

FIG. 22. Dependence of the field components on the longitudinal coordinate for fixed horizontal and vertical coordinates ($Y = -40$ cm, $Z = 20$ cm). The magnetic field components are obtained either with the analytical method (lines) or the numerical method (markers) for different neighboring field map horizontal extensions (90 cm left and 150 cm right). The magnetic field components are similar for both methods, except for the truncation in the numerical method because the neighboring cell field maps have finite extensions.

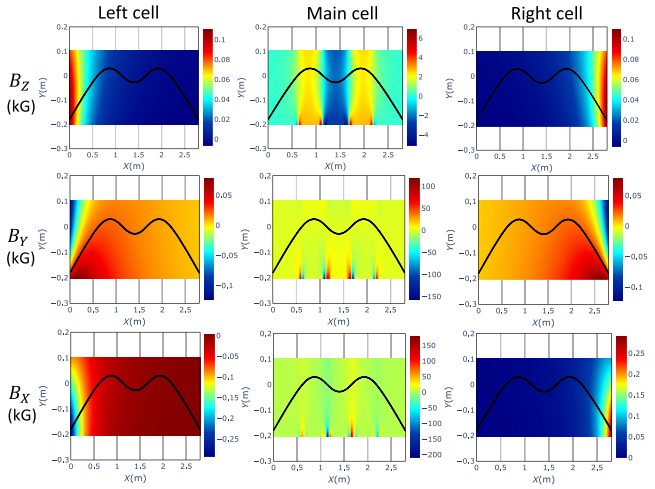

FIG. 23. Magnetic field components for the field maps of the main cell and the neighboring cells. The field maps are represented for $Z = 34$ cm. The additional fields due to the neighboring cells are significant, impacting the main cell optics and closed orbit.

influence of these neighboring cells on the main cell optics properties. Tracking particles in the resulting field map that sums all magnetic fields allows for finding an adequate closed orbit with zero vertical divergence at both ends.

2. Tracking in one cell of the FETS-vFFA with ZGOUBI

Once the field maps of the neighboring elements are computed, ZGOUBI can track particles using the TOSCA keyword. The FETS-vFFA cells are rectangular, leading to a partial overlap of the corresponding rectangular field maps because of the rotation between consecutive cells. To account for the polar character of the machine, it is essential to integrate in polar sectors defined by appropriate

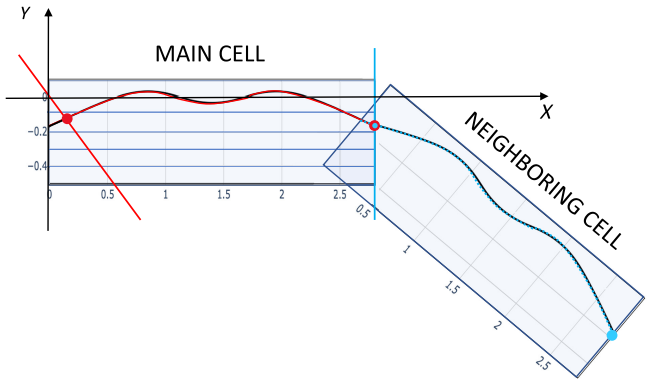

FIG. 24. Representation of two consecutive cells with the integration limits used to track in polar sectors inside the main cell. ZGOUBI tracks particles between the entry integration limit ($\tanh \theta X + Y = 0$) shown in red and the exit integration limit shown in blue, allowing no integration overlap between consecutive elements. The start and end of integration are defined similarly in SCODE.

integration limits. The ZGOUBI TOSCA keyword offers the possibility to fix integration limits. To correctly track particles into the FETS-vFFA cell, we imposed integration limits to avoid overlaps between consecutive cells, as shown in Fig. 24, and ensure the trajectory continuity between neighboring cells.

3. Closed orbit and eigentunes convergence with the neighboring cell field map extensions

We performed a convergence study to see how neighboring cells affect the optical properties of the main cell when the neighboring field maps are extended. For this study, we used truncated field maps created with the numerical method with steps size mesh of ($dX = 0.5$ cm, $dY = 0.5$ cm, and $dZ = 0.5$ cm) and an integration step of 0.2 cm. The neighboring field maps with longitudinal and horizontal extensions of 220 and 180 cm completely cover the closed orbit of the main cell, as shown in Fig. 25. The optical parameters obtained for these field map extensions should be the convergence values, as increasing the field map extensions further should not influence the cell optics. We have computed the optical parameters using field maps with a longitudinal extension of 220 cm but different horizontal extensions to variate the neighboring cell influence.[5] If the neighboring field map horizontal extensions are smaller than 180 cm, the closed orbit will cross its borders at different places, as shown in Fig. 25. As we

[5]Caution should be exercised when considering the magnetic field far from the median plane, as the field is slightly altered because of the truncation of the out-of-plane expansion at the tenth order [16]. While the residual fields may not be completely accurate, we assume that the possible error introduced due to the field truncation is not too significant since the effect of these residual fields becomes increasingly smaller.

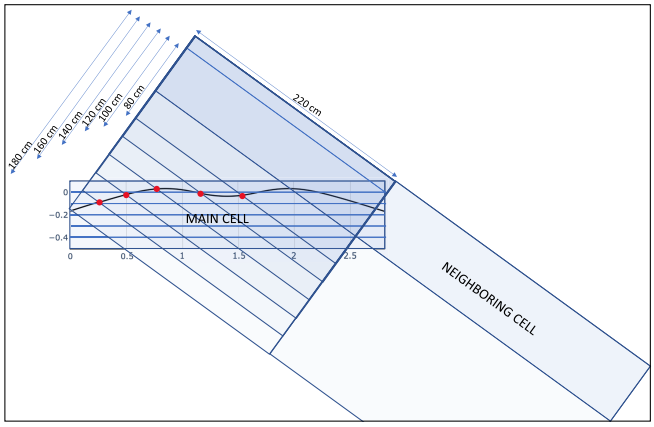

FIG. 25. Illustration of the procedure to study the convergence of the main cell closed orbit and optical parameters with the increasing influence of the neighboring cells. It involves tracking particles in the main cell field map superimposed with neighboring cell field maps with different horizontal extensions. The closed orbit is entirely covered for longitudinal and horizontal extensions of 220 and 180 cm.

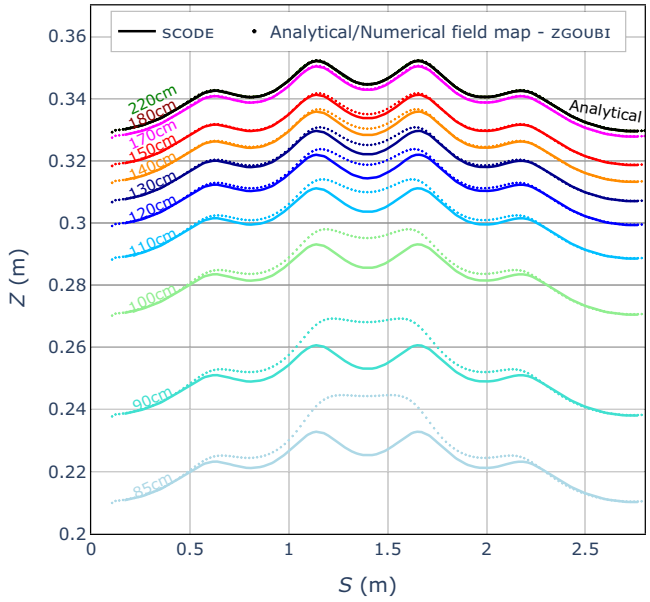

FIG. 26. Closed orbits for different horizontal extensions of the neighboring cell field maps. The colored dashed lines represent the closed orbit found using the field map with finite extents constructed with the numerical method, while the black dashed line indicates the closed orbit found with the analytically computed field maps. The closed orbit found with SCODE in the design stage is represented with solid lines and replicated at several vertical positions to compare its shape and vertical extension with those of the orbits found with ZGOUBI. The closed orbits converge with the neighboring cell field map horizontal extensions toward the analytical field map closed orbit, similar to the SCODE orbit.

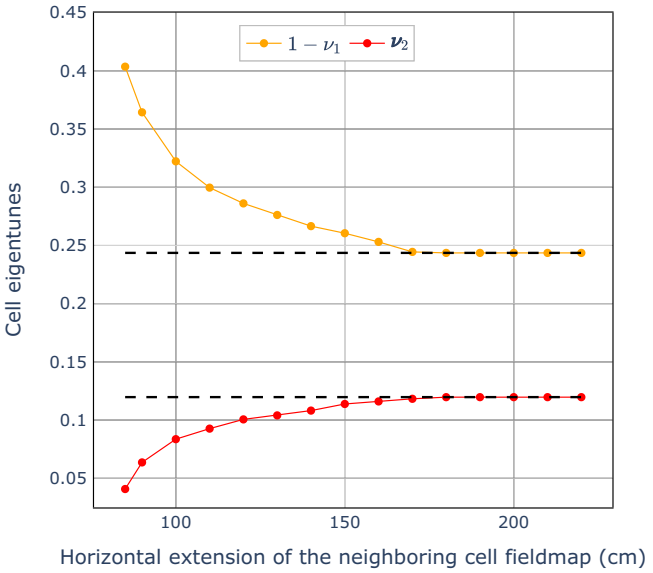

FIG. 27. Dependence of the eigentunes on the horizontal extension of the neighboring cell field maps, hence on the increasing influence of neighboring cells. The tunes are computed from the eigenvalues of the one-cell 4×4 periodic transfer matrix. Convergence is obtained for sufficiently large neighboring cell field map horizontal sizes; the eigentunes converge toward the values obtained with analytically computed field maps (0.24362, 0.119732), indicated by the black lines. These values are similar to those obtained with SCODE (0.243445, 0.12002) in the design stage.

increase the horizontal size of the neighboring field map, the residual fields considered become more significant, with an increasing impact on the main cell closed orbit and linear parameters. In addition, we also computed the cell closed orbit and linear parameters for the field map obtained with the analytical method; the cell optics should converge toward these values.

We obtained closed orbits that converge with the neighboring field map extensions toward the orbit found with the analytical field map, as shown in Fig. 26. The closed orbits obtained for horizontal extensions from 180 cm onward are superimposed with the orbit found for the analytical field map, as expected (the neighboring numerical field maps then entirely cover the closed orbit region). This closed orbit is similar to the one obtained with SCODE during the design stage [14]. The SCODE closed orbit is represented with solid lines in Fig. 26 and is replicated at various vertical coordinates to facilitate comparison of its shape and vertical extension. The closed orbit shape is significantly affected by the additional residual fields, highlighting the importance of accurately modeling the magnet fringe fields. Considering additional neighboring cell fields impacts the closed orbit vertical extension and leads to a vertical orbit excursion.

We performed a similar convergence study for the cell eigentunes, which correspond to the arguments of each

conjugate pair of eigenvalues of the one-cell 4×4 periodic transfer matrix. In Fig. 27, we observe the dependence of the cell eigentunes on the neighboring cell field map horizontal extensions. The eigentunes converge toward those obtained with the analytically constructed field maps (indicated by black lines in Fig. 27), corresponding to $(1-\nu_1, \nu_2) = (0.24362, 0.119732)$. These values are similar to those computed with SCODE (0.243445, 0.12002) [14]. The tune differences between SCODE and ZGOUBI are smaller than 10^{-3}, which is acceptable as it could be explained by the influence of other simulation parameters (including the field map mesh size).

The neighboring cell residual field influence on linear parameters, such as the tunes has already been observed in vFFA lattices with the fringe fields modeled by hyperbolic tangent functions [16]. It is even more significant in the case of the arctangent fringe fields as it also greatly impacts the closed orbit. The convergence of the closed orbit and eigentunes with the neighboring cell field map extension to the results obtained with the analytically computed field maps validates the capacity of the analytical method to model the FETS-vFFA cell accurately. Moreover, the converged values agree with SCODE results. All results in this work are obtained with the analytical method to construct field maps, using ZGOUBI for particle tracking and ZGOUBIDOO to analyze the resulting tracking data.

[1] T. Ohkawa, FFAG electron cyclotron, Bull. APS **30**, 20 (1955).

[2] G. Leleux, J. Proy, and M. Salvat, F.F.A.G. Helicoïdal etude de la stabilite betatron, Service de Physique Appliquee, Section D'Optique Corpusculaire, CEA Saclay Technical Report Rapport O. C. 70, 1959.

[3] J. Teichmann, Accelerators with vertically increasing field, Sov. J. At. Energy **12**, 507 (1963).

[4] S. Brooks, Vertical orbit excursion fixed field alternating gradient accelerators, Phys. Rev. ST Accel. Beams **16**, 084001 (2013).

[5] T. Ohkawa, *Proc. Annual meeting of JPS (1953)* (unpublished).

[6] K. R. Symon, D. W. Kerst, L. W. Jones, L. J. Laslett, and K. M. Terwilliger, Fixed-field alternating-gradient particle accelerators, Phys. Rev. **103**, 1837 (1956).

[7] A. Kolomensky and A. Lebedev, *Theory of Cyclic Accelerators* (North-Holland, Amsterdam, 1966), p. 332.

[8] S. Machida, D. J. Kelliher, J.-B. Lagrange, and C. T. Rogers, Optics design of vertical excursion fixed-field alternating gradient accelerators, Phys. Rev. Accel. Beams **24**, 021601 (2021).

[9] J. Thomason *et al.*, ISIS II "Working Group Report," https://www.isis.stfc.ac.uk/Pages/isis-iiworking-group-report16266.pdf.

[10] C. M. Warsop *et al.*, Studies for major ISIS upgrades via conventional RCS and accumulator ring designs, in *Proceedings of 9th International Particle Accelerator Conference, IPAC-2018, Vancouver, BC, Canada* (JACoW Publishing, Geneva, Switzerland, 2018), pp. 1148–1150.

[11] J.-B. Lagrange *et al.*, Progress on design studies for the ISIS II upgrade, in *Proceedings of 10th International Particle Accelerator Conference, IPAC-2019, Melbourne, Australia* (JACoW Publishing, Geneva, Switzerland, 2019), pp. 2075–2078.

[12] S. Machida, FFA options for ISIS upgrade and the feasibility study, in *Proceedings of 3rd J-PARC Symposium, J-PARC2019* (Physical Society of Japan, Tsukuba, Japan, 2021), p. 011005.

[13] A. P. Letchford *et al.*, Status of the RAL front end test stand, in *Proceedings of 6th International Particle Accelerator Conference, IPAC'15, Richmond, VA* (JACoW Publishing, Geneva, Switzerland, 2015), pp. 3959–3961.

[14] S. Machida, Optics design of VFFA, *International Workshop on Fixed Field alternating gradient Accelerators (FFA'21), Kyoto, Japan* (2021).

[15] M. Vanwelde, C. Hernalsteens, S. A. Bogacz, S. Machida, and N. Pauly, Parametrizations of coupled betatron motion for strongly coupled lattices, J. Instrum. **18**, P10012 (2023).

[16] M. Vanwelde, C. Hernalsteens, F. Méot, N. Pauly, and R. Tesse, Modeling and implementation of vertical excursion FFA in the Zgoubi ray-tracing code, Nucl. Instrum. Methods Phys. Res., Sect. A **1047**, 167829 (2023).

[17] J.-B. Lagrange, VFFA magnet prototype, *International Workshop on Fixed Field alternating gradient Accelerators (FFA'21), Kyoto, Japan* (2021).

[18] M. Vanwelde, C. Hernalsteens, E. Gnacadja, E. Ramoisiaux, N. Pauly, and R. Tesse, 4D Dynamic aperture studies for vertical fixed field accelerators, in *Proceedings of 14th International Particle Accelerator Conference, IPAC-2023, Venice, Italy* (JACoW Publishing, Geneva, Switzerland, 2023).

[19] M. Topp-Mugglestone, J.-B. Lagrange, S. Machida, and S. L. Sheehy, Studies of the vertical excursion fixed field alternating gradient accelerator, in *Proceedings of the 13th International Particle Accelerator Conference, IPAC-2022, Bangkok, Thailand* (JACoW Publishing, Geneva, Switzerland, 2022), pp. 535–538.

[20] M. Topp-Mugglestone, Analytic modelling of the VFFA, *International Workshop on Fixed Field alternating gradient Accelerators (FFA'21), Kyoto, Japan* (2021).

[21] F. Méot, The ray-tracing code Zgoubi, Nucl. Instrum. Methods Phys. Res., Sect. A **427**, 353 (1999).

[22] F. Méot, The ray-tracing code Zgoubi–status, Nucl. Instrum. Methods Phys. Res., Sect. A **767**, 112 (2014).

[23] F. Méot and J. Berg, Zgoubi (2020), http://sourceforge.net/projects/zgoubi/.

[24] C. Hernalsteens, R. Tesse, and M. Vanwelde, Zgoubidoo (2022), https://ulb-metronu.github.io/zgoubidoo/.

[25] M. Vanwelde, C. Hernalsteens, R. Tesse, E. Gnacadja, E. Ramoisiaux, and N. Pauly, The Zgoubidoo Python framework for ray-tracing simulations with Zgoubi: Applications to fixed-field accelerators, J. Phys. Conf. Ser. **2420**, 012039 (2023).

[26] S. Machida, Modelling of a nonscaling FFAG and findings with the new code, ICFA BD Newslett. **43**, 54 (2007).

[27] J.-B. Lagrange, R. Appleby, J. Garland, J. Pasternak, and S. Tygier, Racetrack FFAG muon decay ring for nuSTORM with triplet focusing, J. Instrum. **13**, P09013 (2009).
[28] F. Méot, Zgoubi Users' Guide, Brookhaven National Laboratory Technical Report No. BNL-98726-2012-IR, https://sourceforge.net/p/zgoubi/code/HEAD/tree/trunk/guide/Zgoubi.pdf.
[29] D. Edwards and L. Teng, Parametrization of linear coupled motion in periodic systems, IEEE Trans. Nucl. Sci. **20**, 885 (1973).
[30] I. Borchardt, E. Karantzoulis, H. Mais, and G. Ripken, Calculation of beam envelopes in storage rings and transport systems in the presence of transverse space charge effects and coupling, Z. Phys. C **39**, 339 (1988).
[31] V. Lebedev and S. Bogacz, Betatron motion with coupling of horizontal and vertical degrees of freedom, J. Instrum. **5**, P10010 (2010).
[32] E. Courant and H. Snyder, Theory of the alternating-gradient synchrotron, Ann. Phys. (Paris) **3**, 1 (1958).
[33] M. Giovannozzi and E. Todesco, Numerical methods to estimate the dynamic aperture, Part. Accel. **54**, 203 (1996), https://cds.cern.ch/record/316946/files/p203.pdf.
[34] E. Todesco and M. Giovannozzi, Dynamic aperture estimates and phase-space distortions in nonlinear betatron motion, Phys. Rev. E **53**, 4067 (1996).
[35] A. Bazzani, M. Giovannozzi, and E. H. Maclean, Analysis of the non-linear beam dynamics at top energy for the CERN Large Hadron Collider by means of a diffusion model, Eur. Phys. J. Plus **135**, 77 (2020).
[36] M. Giovannozzi, W. Scandale, and E. Todesco, Dynamic aperture extrapolation in the presence of tune modulation, Phys. Rev. E **57**, 3432 (1998).
[37] L. Bojtár, Frequency analysis and dynamic aperture studies in a low energy antiproton ring with realistic 3D magnetic fields, Phys. Rev. Accel. Beams **23**, 104002 (2020).
[38] F. Pedregosa *et al.*, Scikit-learn: Machine learning in Python, J. Mach. Learn. Res. **12**, 2825 (2011), http://jmlr.org/papers/v12/pedregosa11a.html.
[39] F. Asvesta, N. Karastathis, and P. Zisopoulos, Pynaff: A Python module that implements NAFF (2020), https://github.com/nkarast/PyNAFF.
[40] J. Laskar, C. Froeschlé, and A. Celletti, The measure of chaos by the numerical analysis of the fundamental frequencies. Application to the standard mapping, Physica (Amsterdam) **56D**, 253 (1992).
[41] J. Laskar, Frequency analysis for multi-dimensional systems. Global dynamics and diffusion, Physica D (Amsterdam) **67D**, 257 (1993).
[42] J. Laskar, Frequency map analysis and particle accelerators, in *Proceedings of the 2003 Particle Accelerator Conference PAC-2003, Portland, OR* (IEEE, New York, 2003), pp. 378–382.
[43] A. Meurer *et al.*, Sympy: Symbolic computing in python, PeerJ Comput. Sci. **3**, e103 (2017).